analytical chemistry

pubs.acs.org/ac

Article

Quantum Dot-Based Three-Dimensional Single-Particle Tracking Characterizes the Evolution of Spatiotemporal Heterogeneity in Necrotic Cells

Hong-Yu Luo, Chao Jiang, Shuo-Xing Dou, Peng-Ye Wang,* and Hui Li*

Cite This: *Anal. Chem.* 2024, 96, 11682−11689

Read Online

ACCESS | Metrics & More | Article Recommendations | Supporting Information

ABSTRACT: Cell death is a fundamental biological process with different modes including apoptosis and necrosis. In contrast to programmed apoptosis, necrosis was previously considered disordered and passive, but it is now being realized to be under regulation by certain biological pathways. However, the intracellular dynamics that coordinates with cellular structure changes during necrosis remains unknown, limiting our understanding of the principles of necrosis. Here, we characterized the spatiotemporal intracellular diffusion dynamics in cells undergoing necrosis, using three-dimensional single-particle tracking of quantum dots. We found temporally increased diffusion rates in necrotic cells and spatially enhanced diffusion heterogeneity in the cell periphery, which could be attributed to the reduced molecular crowding resulting from cell swelling and peripheral blebbing, respectively. Moreover, the three-dimensional intracellular diffusion transits from strong anisotropy to nearly isotropy, suggesting a remodeling of the cytoarchitecture that relieves the axial constraint on intracellular diffusion during necrosis. Our results reveal the remarkable alterations of intracellular diffusion dynamics and biophysical properties in necrosis, providing insight into the well-organized nonequilibrium necrotic cell death from a biophysical perspective.

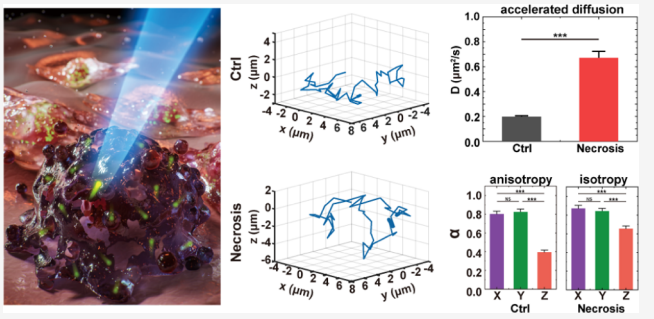

INTRODUCTION

Cell death, as a fundamental biological process, has different forms and pathways, in which apoptosis and necrosis are two major representatives.[1,2] Apoptosis, known as programmed cell death, is characterized by a series of cell morphological changes and enzyme-dependent biochemical processes.[3,4] In contrast, necrosis has traditionally been considered a passive and disordered form of cell death. Recent studies have revealed that necrosis occurs not only in pathological situations but also in some physiological contexts.[5] Furthermore, researchers have observed that necrosis is associated with activation of signaling pathways and can be inhibited by specific enzymes.[6−9] These findings challenge the conventional understanding of uncontrolled necrosis, leading to new investigations of necrotic mechanisms and functioning.[10] Cell death is not only regulated by biological signals but also closely associated with changes in biophysical properties in cell.[4,11,12] For example, in apoptotic cells, intracellular transport is accelerated at an early stage as a result of elevated adenosine 5′-triphosphate (ATP) levels,[13] while intranuclear diffusion is reduced in the execution stage due to nuclear condensation.[14] In necrotic cells, structural changes[15] including cell swelling, cellular lysis, and plasma membrane rupture would also significantly impact the intracellular environment and dynamics, collectively coordinating the progress of necrosis.[16−19] However, the spatiotemporal characteristics of the physical properties within cells undergoing necrosis remain unclear, limiting our understanding of the principle of necrosis.

Considering the dramatic morphological changes over time for cell necrosis, a method to characterize the spatiotemporal heterogeneity of intracellular environments is needed.[20−22] Compared with conventional techniques for intracellular dynamics based on ensemble-average, including fluorescence recovery after photobleaching and fluorescence correlation spectroscopy,[23] the single particle tracking (SPT) method enables the direct measurement of dynamic behaviors for individual probes from their trajectories, with nanometer-scale spatial and millisecond-scale temporal resolution.[24−26] It provides not only dynamic information about the probes but also infers the properties of the microenvironment experienced by the probes.[20,25−27] Moreover, to faithfully follow the evolution of necrosis with cell swelling in which the changes in cell heights are noticeable, the three-dimensional (3D) SPT

Received: January 5, 2024
Revised: June 28, 2024
Accepted: July 2, 2024
Published: July 9, 2024

https://doi.org/10.1021/acs.analchem.4c00097
Anal. Chem. 2024, 96, 11682−11689

is needed to comprehensively determine the intracellular dynamics in three directions.[28,29] In addition, quantum dots (QDs) as an emerging fluorescent probe with high photostability and excellent biocompatibility could serve as an ideal tracer for the long-time necrotic process.[30−34] By combining these advanced experimental techniques and biophysical measurements, complex intracellular diffusion dynamics associated with necrosis can be revealed comprehensively.

Here, by using the 3D long-time SPT of QDs in living cells, we characterized the spatiotemporally intracellular diffusion dynamics during necrosis. We observed temporally increasing diffusion rates and spatially enhancing heterogeneity of the diffusion map in single cells undergoing necrosis. Moreover, a transition from anisotropic to isotropic diffusion modes was found in necrosis. These changes in intracellular diffusion dynamics are coordinated with cell morphological alterations by dynamical blebbing and volume swelling, indicating a gradually evolved intracellular environment during necrosis. Our biophysical study reveals a well-organized nonequilibrium process of cell necrosis, and contributes to a better understanding of the principles governing necrotic cell death.

EXPERIMENTAL SECTION

Cell Culture and Drug Treatment. Human lung carcinoma A549 cells (ATCC) were cultured in Dulbecco's modified Eagle's medium (DMEM, GIBCO) supplemented with 10% fetal bovine serum (FBS, GIBCO) and 1% penicillin−streptomycin (GIBCO) at 37 °C with 5% CO_2. One day prior to the experiments, cells in the exponential growth phase were seeded in a Petri dish with a cover-glass bottom. To induce necrosis, the cells were treated with 20 mM hydrogen peroxide. After approximately 30 min, cell swelling and blebbing could be observed. The cytoplasm of cells was stained by CellTracker Deep Red (C34565, Invitrogen) or CellTracker Green CMFDA (C7025, Invitrogen), and the nucleus was stained by Hoechst 33342 (Invitrogen). The actin filament was stained by SiR-actin Kit (CY-SC001, Cytoskeleton), and the endoplasmic reticulum (ER) was stained by mEmerald-ER5 plasmid (a gift from Junjie Hu's lab) by using Lipofectamine 3000 (L3000001, Invitrogen). The actin filament was disrupted by 1 μM cytochalasin D for 30 min, and the ER structure was disrupted by 2 μg/mL ionomycin for 20 min. To observe the change in membrane permeability, 0.1 μg/mL propidium iodide (PI) was added to the cell culture medium. Chemical reagents were from Sigma-Aldrich unless otherwise stated.

QDs Internalization in Living Cells. The quantum dots 655 (Q10121MP, Invitrogen) and 2000-kDa tetramethylrhodamine-dextrans (D7139, Invitrogen) were loaded into the cytoplasm of cells through the osmotic lysis of pinocytic vesicles (I-14402, Invitrogen). Briefly, a hypertonic solution containing 0.5−5 nM QDs or 0.2−0.5 mg/mL dextrans was added to the cells and incubated for 10 min at 37 °C to facilitate the internalization of the probes within pinocytic vesicles. Subsequently, the cells were incubated in a hypotonic solution for 2 min to release the probes into the cellular cytoplasm via the burst of pinocytic vesicles. Finally, the cells were maintained in complete DMEM at 37 °C for 15 min for recovery before imaging.

Microscope. Wide-field and highly inclined and laminated optical sheet (HILO) fluorescence imaging of QDs was conducted using an Olympus fluorescence microscope (IX73) equipped with a 60× oil-immersion objective (1.45 NA) and a back-illuminated EMCCD camera (DU-897 Ultra, Andor Technology). QDs and tetramethylrhodamine-dextrans were excited by a 561 nm laser (Sapphire 561, Coherent). A mechanical shutter (Uniblitz LS6T2, Vincent Associates) was used to control the on−off state of the laser. To maintain the physiological state for the living cells, an on-stage chamber (Tokia Hit) was used to provide the conditions of 37 °C and 5% CO_2. The two-dimensional (2D) diffusion of QDs was recorded at 100 Hz for 2000 frames, taken every 10 min since the necrosis induction. The 2D diffusion of dextran was recorded at 33 Hz for 2000 frame. For 3D SPT tracking of QDs, the emission light signal was divided into two beams with a 3:7 intensity ratio by a dual-view imaging system (DV2, Photometrics). A lens with a focal length of 400 mm was inserted into the beam path with 70% intensity, for the capture of a defocused image of the particles with diffraction rings. To calibrate the relationship between the z position of particles and the radius of the diffraction rings, a piezoelectric stage was employed. Considering the signal intensities, the 3D diffusion of QDs was recorded at 33 Hz to improve signal-to-noise ratio, for 2000 frames, taken every 10 min since the necrosis induction. For cell morphological imaging, a commercial confocal microscope (Leica SP8 with a 40× 1.3 NA and oil-immersed objective) was used.

2D Single-Particle Tracking. The tracking was conducted using the ImageJ plugin Particle Tracker. Typically, in each frame, individual particles were localized by adjusting the radius and percentile parameters to capture the maximum number of genuine particles. During the linking process, the same particles in consecutive frames were identified and connected based on the parameters of linking range and displacement, which were chosen to be 2 and 2, respectively. This criterion allows the detection and linking of particles that appeared within a span of no more than 2 frames and exhibited movement of less than 2 pixels within a single frame. Only the trajectories longer than 30 frames were selected for further dynamical analysis.

3D Single-Particle Tracking. To accurately determine the 3D positioning of single particles, a combination of in-focused and off-focused images was utilized. The x and y coordinates were determined from the in-focused images, using the same method employed for 2D. The z coordinates were determined from the diffraction rings in off-focus images. To calibrate between the diffraction ring radius and the z position of a QD, a piezoelectric stage was utilized to displace the Petri dish along the axis by 50 nm every 5 s, and simultaneously, immobilized QDs located at the glass bottom were imaged. By performing a linear fitting of the ring radius and the displacement of the piezoelectric stage, the calibration relationship between the ring radius and z position was obtained. Consequently, the z coordinates of the QDs could be determined using this calibration curve. The calibrations were determined in each experiment. The diffraction ring detection and fitting were performed by a user-defined program in Matlab.

Dynamical Analysis. Trajectory analysis was performed utilizing a customized program in Matlab. First, to remove the immobilized probes, trajectories with the displacement smaller than 0.5 pixels (equivalent to 0.1333 μm) were excluded. The mean square displacement (MSD) for each trajectory was calculated by $\mathrm{MSD}(\tau) = \langle |r(t+\tau) - r(t)|^2 \rangle$, where τ represents the time lag. The exponent α was derived through a nonlinear fitting approach: $\mathrm{MSD}(\tau) = A\tau^{\alpha}$, and the diffusion rates D were

https://doi.org/10.1021/acs.analchem.4c00097
Anal. Chem. 2024, 96, 11682−11689

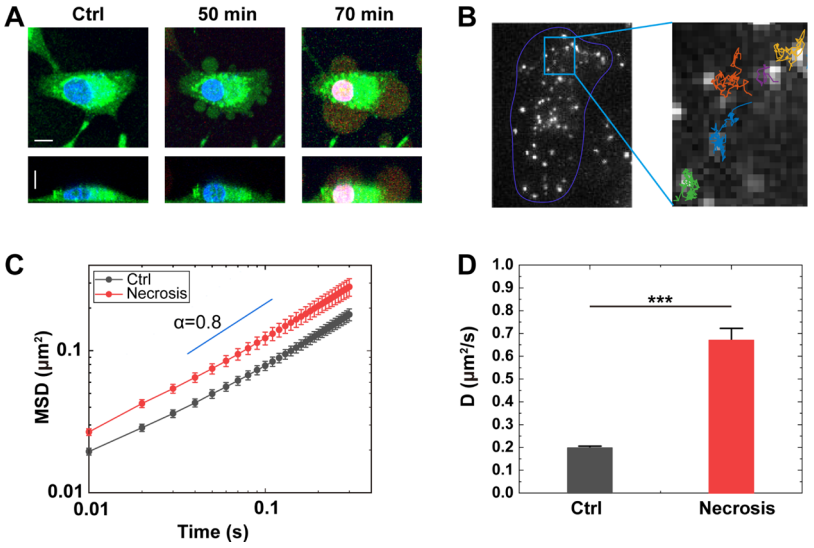

Figure 1. Intracellular diffusion of QDs is enhanced in necrotic cells. (A) Fluorescent images of an A549 cell undergoing necrosis. Top view (upper panels), side view (lower panels). The cytoplasm is labeled by CellTracker (green) and the nucleus is labeled by Hoechst 33342 (blue). Propidium iodide (red) was added to indicate the cell membrane permeability. Scale bar, 10 μm. (B) Fluorescent image of the QDs diffusing in the cytoplasm (left), with their trajectories shown in different colors (right). (C) Comparison of the mean MSD curves for QDs in control and necrotic cells. (D) Comparison of the diffusion rates D for QDs in control and necrotic cells. The necrotic cells treated with H_2O_2 for 60 min. Ctrl, 5 cells, 2563 trajectories; necrosis, 5 cells, 217 trajectories. ***P < 0.001. Error bars indicate the standard error of the mean (SEM).

calculated through the linear fitting approach, $\mathrm{MSD}(\tau) = 2kD\tau$, where k represents the number of dimensions measured. Specifically, an α value close to 1 indicates Brownian motion, while values below 1 suggest subdiffusion. Considering the similar α between normal cells and necrotic cells, it is acceptable to compare diffusion dynamics by diffusion rates D.

Spatial Analysis. The maps of diffusion rates D and exponent α were plotted using a user-defined program in Matlab. Initially, the cell area was divided into a grid of 2 by 2 pixels. At each grid intersection, the average values of D and α were calculated based on the segments of the tracks within a circular area with a radius of 1.5 pixels. Briefly, the spatially local MSD for each grid point was calculated using these trajectory segments, and then the local diffusion rates D and exponent α were determined by fitting the local MSD curves with the same equations shown above. The D and α maps were plotted in Matlab, with a built-in smoothing process.

Measurements of Cell Morphological Parameters. The cells were stained by CellTracker and images under a Leica SP8 confocal microscope. The ImageJ plugin 3D Objects Counter was utilized for measuring cell volume. Initially, individual cells were extracted using the 3D Viewer tool. Subsequently, an appropriate and uniform threshold was selected to accurately measure the volume of cells. To determine the cell area, a stack of all layers was created by superimposing all cell images. The area measurement was then performed on this stacked image, providing an accurate representation of the total cell area. For the measurement of cell height, the vertical distance between the highest and lowest points of the cellular image in three dimensions was calculated. This distance accurately reflects the height of the cells under investigation.

Image Processing. All image processing tasks were conducted using the ImageJ software. The cell boundaries were manually determined in the bright-field images.

Statistics. Comparisons were performed using a two-sample t test in Origin software: *P < 0.05; **P < 0.01; ***P < 0.001; NS, not significant. All the measurements were taken in more than three independent experiments.

RESULTS AND DISCUSSION

To induce necrosis in A549 cells, we applied excess oxidative stress by adding 20 mM hydrogen peroxide to the culture medium.[35] It shows that bleb formation occurs on the cell membrane and enlarges over time, and the nucleus remains morphologically unfragmented (Figures 1A and S1).[3,15] After excessive blebbing and remarkable swelling, the plasma membrane becomes ruptured, as indicated by propidium iodide (PI) signals at the nucleus. These phenomena suggest the occurrence of necrosis in our experiments,[36] which is obviously distinct from the apoptotic features with fragmented nucleus and integrated plasma membrane (Figures S2 and S3). In order to measure the diffusion of QDs within necrotic cells, QDs were loaded into the cytosol using the osmotic lysis of pinocytic vesicles,[37−39] prior to the induction of necrosis. Considering the possible toxicity of QDs,[40,41] we examined the cell proliferation and death rates, and found that the loaded QDs have no influence on the cell viability (Figure S4). The diffusion of QDs was recorded at a rate of 100 Hz for 20 s, every 10 min during the progress of necrosis. To analyze the diffusion dynamics, trajectories of the QDs were first extracted from the videos (Figure 1B), and then the mean square displacement (MSD) was calculated by $\mathrm{MSD}(\tau) = \langle |r(t+\tau) - r(t)|^2 \rangle$, where τ is the time lag.[27,30] By fitting MSD with the nonlinear equation $\mathrm{MSD} = At^{\alpha}$, we could determine the exponent α, which is an indicator of anomalous diffusion.[25,30] The diffusion rates D are determined by linear fitting of the first three points of MSD by $\mathrm{MSD} = 2kDt$, where k is the number of dimensions.[25,30] We observed a significant increase in MSD of intracellular QDs for necrotic cells with blebbing, with the diffusion rates increasing from 0.198 to 0.670 $\mu m^2/s$, while the α remains similar (~0.8) (Figures 1C,D and S5). It is known that the diffusion rate in cells is largely hindered by molecule crowding compared with that in solution. These

https://doi.org/10.1021/acs.analchem.4c00097
Anal. Chem. 2024, 96, 11682−11689

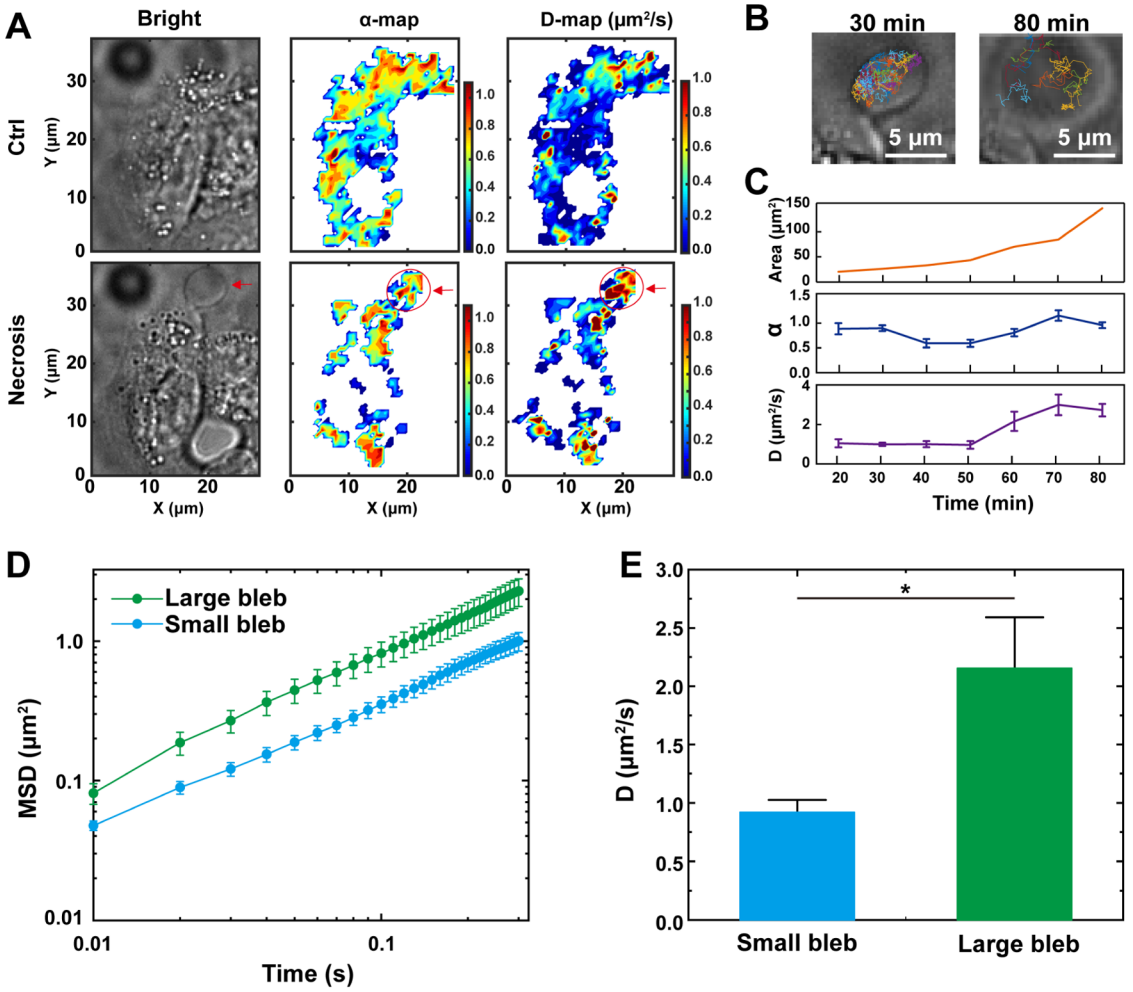

Figure 2. Spatial characteristics of intracellular diffusion in necrotic cells. (A) Comparison of exponent α and diffusion rate D maps for diffusing QDs in single cells. The shown necrotic cell was at 50 min after the H_2O_2 treatment. Red circles and arrows indicate the location of a necrotic bleb. (B) Images of the necrotic bleb at 30 min (left) and 80 min (right) after hydrogen peroxide treatment. The QD trajectories were plotted in different colors. (C) The bleb area, and the average exponent α and diffusion rates for QDs diffusing inside the bleb, at different time points after treatment. (D) MSD for QDs in small blebs (<50 μm^2) and large blebs (>100 μm^2). (E) Average diffusion rates for QDs in small blebs (n = 11, containing 132 trajectories) and large blebs (n = 12, containing 161 trajectories). *P < 0.05. Error bars indicate the SEM.

results suggest that the intracellular environment underwent a profound alteration with reduced molecule crowding, likely resulting from the obvious swelling of necrotic cells.[25,42] To exclude the possible influence of the QDs on intracellular diffusion, we used 2000-kDa tetramethylrhodamine-dextrans as the nonspecific probes and observed similar results (Figure S6). Moreover, these phenomena could also be observed in HeLa cells, suggesting the universality of the increased intracellular diffusion in necrotic cells (Figure S7).

With cell swelling and bleb formations, necrotic cells show distinct changes in morphology.[43] To further investigate the spatial characteristics of intracellular diffusion dynamics associated with these morphological alterations, the diffusion map was plotted, showing the local diffusion rates at each point within the cell.[20,44] Briefly, the cell area was divided into a grid, and at each grid point, the local D and exponent α were calculated from the segments of the trajectories around the point. Interestingly, we found that the diffusion map becomes more heterogeneous during cell necrosis, with obviously increased D values emerging at the newly formed bleb regions (Figures 2A and S8). Subsequently, we made a close analysis of QD trajectories within the bleb. It is shown that, with the gradually enlarging size of the bleb, the diffusion rates of QDs increase accordingly. Thus, a positive correlation between the intracellular diffusion rates and the bleb sizes is observed (Figure 2B,C). To further verify this, a statistical comparison was made between the small (<50 μm^2) and large blebs (>100 μm^2), showing a significant increase in intracellular diffusion rates (0.92 ± 0.10 $\mu m^2/s$) for the larger blebs compared to that (2.16 ± 0.43 $\mu m^2/s$) for smaller blebs (Figure 2D,E). The increasing intracellular diffusion rates with the bleb sizes indicate a gradually reduced molecular crowding inside the blebs, which could be attributed to the influx of water through the plasma membrane.[45] Along with more bleb formation, the cell periphery shows faster intracellular diffusion compared with the perinuclear region. Collectively, our results suggest that intracellular diffusion is more spatially heterogeneous in necrotic cells, resulting from the peripheral blebbing.

The intracellular diffusion mentioned above is measured by two-dimensional SPT. However, considering the substantial swelling of necrotic cells, a three-dimensional SPT of QDs in cells was needed to characterize the changes of intracellular properties in the axial direction. To do so, we used two-focal imaging to capture the diffraction ring of QDs. The axial

https://doi.org/10.1021/acs.analchem.4c00097
Anal. Chem. 2024, 96, 11682−11689

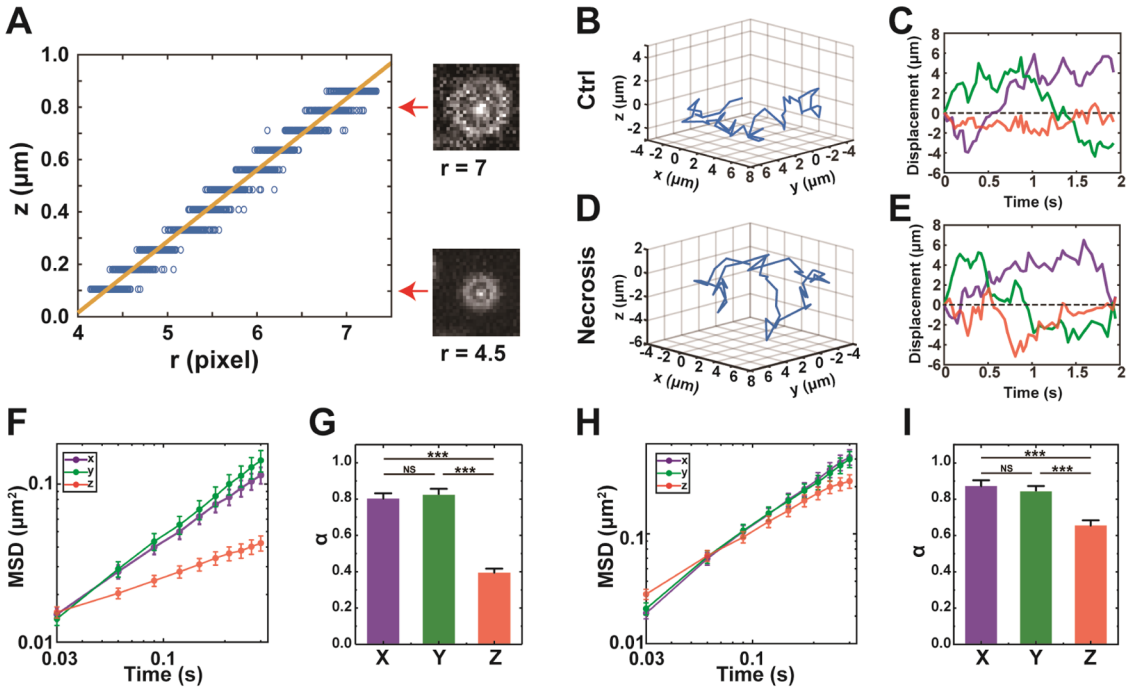

Figure 3. 3D SPT reveals an intracellular diffusion mode transition from anisotropic to nearly isotropic diffusion during necrosis. (A) Calibrated relationship between the axial location (z) and the diffraction ring radius (r). The yellow line represents a linear fit of the data, yielding $z = -0.107 + 0.273r$. The right panel shows representative fluorescent images of diffraction rings of a QD with a radius of 7 and 4.5 pixels, respectively. Pixel size, 0.2667 μm. (B) A representative 3D trajectory for a QD in control cells. (C) The displacement in x, y, and z directions over time for the trajectory shown in (B). (D) A representative 3D trajectory for a QD in necrotic cells. (E) The displacement in x, y, and z directions over time for the trajectory shown in (D). (F) Average MSD of QDs in control cells in one dimension (x, y, and z). (G) Average α of QDs in control cells in one dimension (x, y, and z). (H) Average MSD of QDs in necrotic cells in one dimension (x, y, and z). (I) Average α of QDs in necrotic cells in one dimension (x, y, and z). Sample size: ctrl (7 cells, 904 trajectories), necrosis (13 cells, 549 trajectories). ***$P < 0.001$; NS, not significant. Error bars indicate the SEM.

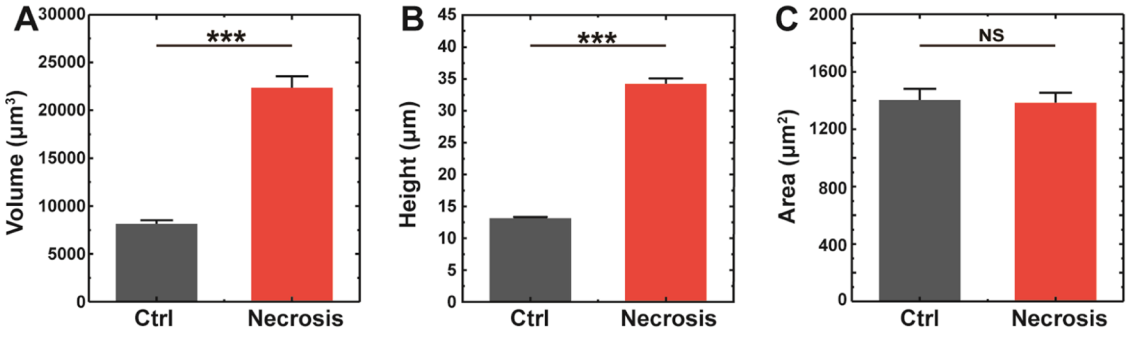

Figure 4. Quantification of cell morphological parameters in control and necrotic cells. Cell volume (A), height (B), and spreading area (C) for control and necrotic cells. The cells were labeled by CellTracker and then imaged under a confocal microscope. These morphological parameters are analyzed from the 3D images of cells. Ctrl, 20 cells; necrosis, 20 cells; ***$P < 0.001$; NS, not significant. Error bars indicate the SEM.

location of the QD is determined by the radius of the diffraction ring for the QD, with a calibrated relationship between them (Figure 3A).[21,46] In control cells, the diffusion of QDs is mainly in the lateral direction and restricted in the axial direction, in agreement with a previous report for quasi-2D diffusion (Figure 3B,C).[46] Notably, in necrosis cells, the axial diffusion of QDs becomes motile, with the range of QD motion in the z-direction approaching those in the x and y directions (Figure 3D,E). The MSD curve further illustrates the distinct differences in the axial direction between the control and necrotic cells (Figure 3F–I). The α in the z direction increases from 0.4 to 0.63 after cellular necrosis, while the lateral diffusion only has a slight increase in the α values, indicating the axially constrained motion is obviously relieved in the necrotic cells. Together, our results reveal an intracellular diffusion mode transition from strong anisotropic to nearly isotropic diffusion, suggesting a remodeling in the 3D cytoarchitecture during the cellular physiological state change from control to necrosis.

The remarkably increased intracellular diffusion and altered 3D diffusion mode imply that the cytoplasmic environment and its physical properties underwent a profound alteration during necrosis.[39,47] Considering the complexity of cell necrosis process, multiple factors may be involved in intracellular diffusion.[15] We first checked the actin filament as it is closely correlated with intracellular transport dynamics and tends to reorganize under various physiological circumstances.[48] We observed a slight rearrangement of the actin

https://doi.org/10.1021/acs.analchem.4c00097
Anal. Chem. 2024, 96, 11682−11689

filaments in necrotic cells (Figure S9), consistent with previous reports.[49,50] We further disrupted the actin filament with cytochalasin D, and the diffusion coefficient of QDs did not change significantly (Figure S10). This suggests the actin filament cytoskeleton is irrelevant to the intracellular diffusion in necrotic cells. Second, we examined the endoplasmic reticulum (ER), as it is associated with the intracellular diffusion.[20] The ER becomes fragmented after necrosis (Figure S11). Thus, we measured QD diffusion in cells with fragmented ER induced by ionomycin, and found the about 49% increase of diffusion rates (Figure S10). However, we note that the intracellular diffusion rates increase by over 200% in necrotic cells, which is significantly more than that induced by ionomycin. It implies that although the fragmental ER contributes to the increase of intracellular diffusion during necrosis, it is not the dominant factor. Then, we quantified the changes in cell volume, as it is tightly associated with intracellular molecular crowding and thus impacts intracellular diffusion.[39,47] Our results show that necrotic cells have swollen to approximately four times the size of control cells, which could be attributed to the increased cell membrane permeability (Figure 4A). With a mass of water influx from the extracellular environment into necrotic cells, intracellular molecule crowding is greatly attenuated, leading to increased diffusion in necrotic cells.[42] Furthermore, we compared the cell heights and spreading areas and found that the necrotic cell swelling is mainly contributed by the expanded cell height, not the area (Figure 4B,C). Since it is reported that the axial constraint on QD diffusion is the result of laterally distributed subcellular structures, we speculate that the pronounced increase in cell height may impair the layered cytoarchitecture and relieve the physical constraint on the axial diffusion.

CONCLUSIONS

In this study, for the first time, we characterized the 3D spatiotemporal intracellular diffusion dynamics during necrosis using the SPT of QDs. Temporally, we observed accelerated diffusion within necrotic cells, which gradually increased with cell swelling over time. Spatially, we demonstrated enhanced heterogeneity in the diffusion map, with faster diffusion in peripheral regions due to the presence of blebs. Interestingly, we observed a positive correlation between intracellular diffusion rates and bleb sizes. Furthermore, employing the 3D SPT method, we found that axial diffusion becomes mobile after necrosis, in contrast to the axial constraint in control cells, indicating a transition of the 3D diffusion mode from anisotropy to nearly isotropy. Compared with traditional 2D SPT mainly in adherent cells,[51] our 3D SPT extends to the studies of 3D-cultured cells and the 3D cellular behaviors. More importantly, by integrating molecular diffusion dynamics, subcellular blebbing, and cellular death behaviors, our work provides a new way to characterize the spatiotemporal evolutions of complex multiscale biological systems.

The spatiotemporal intracellular diffusion dynamics provide insights into the changes of cytoplasmic properties underlying cellular necrosis. The overall increased diffusion observed in necrotic cells indicates less molecular crowding,[52] as a result of increased cell volume due to necrotic swelling. Moreover, the diffusion in blebs depends on and increases with the bleb sizes, suggesting that the necrotic blebs contain cytoplasmic contents, instead of being solely a liquid environment, which would have a stable intracellular diffusion rate. Furthermore, the isotropic diffusion in necrotic cells implies that the cytoplasmic architecture becomes isotropic, which is quite different from planar-distributed structures in normal adherent cells.[46,53,54] These results are coordinated with the cell morphological alterations during necrosis. Nevertheless, further investigations are necessary to directly explore the ultrafine structures in necrotic cells using advanced imaging and detecting methods.[54−56] Moreover, the metabolic activity also changes in necrotic cells, the role of which in intracellular diffusion needs to resolved.[15]

Previous studies have shown changes in intracellular dynamics and their correlations in cell apoptosis.[13,14] In our study, we observed spatiotemporal heterogeneity in intracellular diffusion rates and identified an isotropic 3D diffusion mode in necrosis cells. These results highlight the importance of intracellular dynamics in cell death behaviors. The evolution of intracellular diffusion characteristics during necrosis reveals a typically nonequilibrium biological process,[57] and, more importantly, contribute to our understanding of necrotic cell death under control.

ASSOCIATED CONTENT

Supporting Information

The Supporting Information is available free of charge at https://pubs.acs.org/doi/10.1021/acs.analchem.4c00097.

Detailed evolution of 3D morphology of necrotic cells, detailed evolution of average D in necrotic cells, distribution of D and α in necrotic cells, impact of QD induction on cells, morphology of apoptotic cells after low-concentration H_2O_2 treatment, cell death rate after H_2O_2 treatment, intracellular diffusion of 2000-kDa tetramethylrhodamine-dextrans in necrotic cells, intracellular diffusion of QDs in necrotic HeLa cells, actin filament and ER structures of necrotic cells, the impact of actin filament and ER disruptions to intracellular diffusion (PDF)

AUTHOR INFORMATION

Corresponding Authors

Peng-Ye Wang − *Beijing National Laboratory for Condensed Matter Physics and Laboratory of Soft Matter Physics, Institute of Physics, Chinese Academy of Sciences, Beijing 100190, China; School of Physical Sciences, University of Chinese Academy of Sciences, Beijing 100049, China; Songshan Lake Materials Laboratory, Dongguan, Guangdong 523808, China*; Email: pywang@iphy.ac.cn

Hui Li − *School of Systems Science and Institute of Nonequilibrium Systems, Beijing Normal University, Beijing 100875, China*; orcid.org/0000-0003-0551-9912; Email: huili@bnu.edu.cn

Authors

Hong-Yu Luo − *Beijing National Laboratory for Condensed Matter Physics and Laboratory of Soft Matter Physics, Institute of Physics, Chinese Academy of Sciences, Beijing 100190, China; School of Physical Sciences, University of Chinese Academy of Sciences, Beijing 100049, China*

Chao Jiang − *Beijing National Laboratory for Condensed Matter Physics and Laboratory of Soft Matter Physics, Institute of Physics, Chinese Academy of Sciences, Beijing 100190, China; School of Physical Sciences, University of Chinese Academy of Sciences, Beijing 100049, China*

Shuo-Xing Dou − *Beijing National Laboratory for Condensed Matter Physics and Laboratory of Soft Matter Physics, Institute of Physics, Chinese Academy of Sciences, Beijing 100190, China; School of Physical Sciences, University of Chinese Academy of Sciences, Beijing 100049, China;* orcid.org/0000-0002-7201-2081

Complete contact information is available at: https://pubs.acs.org/10.1021/acs.analchem.4c00097

Notes

The authors declare no competing financial interest.

■ ACKNOWLEDGMENTS

This study is supported by the National Natural Science Foundation of China (12122402, 12074043, and 12135003) and the Fundamental Research Funds for the Central Universities.

■ REFERENCES

(1) Gudipaty, S. A.; Conner, C. M.; Rosenblatt, J.; Montell, D. J. *Annu. Rev. Cell Dev. Biol.* **2018**, *34*, 311−332.
(2) Denault, J. B.; Salvesen, G. S. *Chem. Rev.* **2002**, *102* (12), 4489−4499.
(3) Elmore, S. *Toxicol. Pathol.* **2007**, *35* (4), 495−516.
(4) Taylor, R. C.; Cullen, S. P.; Martin, S. J. *Nat. Rev. Mol. Cell Biol.* **2008**, *9* (3), 231−241.
(5) Cho, Y. S.; Park, S. Y.; Shin, H. S.; Chan, F. K. *Mol. Cells* **2010**, *29* (4), 327−332.
(6) Festjens, N.; Vanden Berghe, T.; Vandenabeele, P. *Biochim. Biophys. Acta, Bioenerg.* **2006**, *1757* (9−10), 1371−1387.
(7) Golstein, P.; Kroemer, G. *Trends Biochem. Sci.* **2007**, *32* (1), 37−43.
(8) Burgener, S. S.; Leborgne, N. G. F.; Snipas, S. J.; Salvesen, G. S.; Bird, P. I.; Benarafa, C. *Cell Rep.* **2019**, *27* (12), 3646−3656.
(9) Amaral, E. P.; Foreman, T. W.; Namasivayam, S.; Hilligan, K. L.; Kauffman, K. D.; Barbosa Bomfim, C. C.; Costa, D. L.; Barreto-Duarte, B.; Gurgel-Rocha, C.; Santana, M. F.; Cordeiro-Santos, M.; Du Bruyn, E.; Riou, C.; Aberman, K.; Wilkinson, R. J.; Barber, D. L.; Mayer-Barber, K. D.; Andrade, B. B.; Sher, A. *J. Exp. Med.* **2022**, *219* (11), No. e20220504.
(10) Syntichaki, P.; Tavernarakis, N. *EMBO Rep.* **2002**, *3* (7), 604−609.
(11) Yang, N.; Shi, Q.; Wei, M.; Xiao, Y.; Xia, M.; Cai, X.; Zhang, X.; Wang, W.; Pan, X.; Mao, H.; Zou, X.; Guo, M.; Zhang, X. *ACS Nano* **2023**, *17* (21), 21383−21393.
(12) Kong, J.-W.; Dou, S.-X.; Li, W.; Li, H.; Wang, P.-Y. *Chin. Phys. Lett.* **2023**, *40* (7), No. 078701.
(13) Li, B.; Dou, S.-X.; Yuan, J.-W.; Liu, Y.-R.; Li, W.; Ye, F.; Wang, P.-Y.; Li, H. *Proc. Natl. Acad. Sci. U.S.A.* **2018**, *115* (48), 12118−12123.
(14) Pliss, A.; Kuzmin, A. N.; Kachynski, A. V.; Prasad, P. N. *Proc. Natl. Acad. Sci. U.S.A.* **2010**, *107* (29), 12771−12776.
(15) Proskuryakov, S. Y.; Konoplyannikov, A. G.; Gabai, V. L. *Exp. Cell Res.* **2003**, *283* (1), 1−16.
(16) Barros, L. F.; Kanaseki, T.; Sabirov, R.; Morishima, S.; Castro, J.; Bittner, C. X.; Maeno, E.; Ando-Akatsuka, Y.; Okada, Y. *Cell Death Differ.* **2003**, *10* (6), 687−697.
(17) Eida, S.; Van Cauteren, M.; Hotokezaka, Y.; Katayama, I.; Sasaki, M.; Obara, M.; Okuaki, T.; Sumi, M.; Nakamura, T. *Sci. Rep.* **2016**, *6* (1), No. 19051.
(18) Rostami, A.; Lambie, M.; Yu, C. W.; Stambolic, V.; Waldron, J. N.; Bratman, S. V. *Cell Rep.* **2020**, *31* (13), No. 107830.
(19) Dondelinger, Y.; Priem, D.; Huyghe, J.; Delanghe, T.; Vandenabeele, P.; Bertrand, M. J. M. *Cell Death Dis.* **2023**, *14* (11), No. 755, DOI: 10.1038/s41419-023-06284-z.
(20) Li, H.; Dou, S.-X.; Liu, Y.-R.; Li, W.; Xie, P.; Wang, W.-C.; Wang, P.-Y. *J. Am. Chem. Soc.* **2015**, *137* (1), 436−444.
(21) Jiang, C.; Yang, M.; Li, W.; Dou, S.-X.; Wang, P.-Y.; Li, H. *iScience* **2022**, *25* (5), No. 104210.
(22) Fakhri, N.; Wessel, A. D.; Willms, C.; Pasquali, M.; Klopfenstein, D. R.; MacKintosh, F. C.; Schmidt, C. F. *Science* **2014**, *344* (6187), 1031−1035.
(23) Liße, D.; Richter, C. P.; Drees, C.; Birkholz, O.; You, C.; Rampazzo, E.; Piehler, J. *Nano Lett.* **2014**, *14* (4), 2189−2195.
(24) Manzo, C.; Garcia-Parajo, M. F. *Rep. Prog. Phys.* **2015**, *78* (12), No. 124601.
(25) Dix, J. A.; Verkman, A. S. *Annu. Rev. Biophys.* **2008**, *37* (1), 247−263.
(26) Pan, Q.; Sun, D. X.; Xue, J. F.; Hao, J.; Zhao, H. S.; Lin, X. J.; Yu, L.; He, Y. *ACS Nano* **2021**, *15* (1), 539−549.
(27) Metzler, R.; Jeon, J.-H.; Cherstvy, A. G.; Barkai, E. *Phys. Chem. Chem. Phys.* **2014**, *16* (44), 24128−24164.
(28) Dupont, A.; Lamb, D. C. *Nanoscale* **2011**, *3* (11), 4532−4541.
(29) von Diezmann, L.; Shechtman, Y.; Moerner, W. E. *Chem. Rev.* **2017**, *117* (11), 7244−7275.
(30) Bannai, H.; Lévi, S.; Schweizer, C.; Dahan, M.; Triller, A. *Nat. Protoc.* **2006**, *1* (6), 2628−2634.
(31) Pinaud, F.; Clarke, S.; Sittner, A.; Dahan, M. *Nat. Methods* **2010**, *7* (4), 275−285.
(32) Clausen, M. P.; Lagerholm, B. C. *Nano Lett.* **2013**, *13* (6), 2332−2337.
(33) Wang, Z. G.; Liu, S. L.; Pang, D. W. *Acc. Chem. Res.* **2021**, *54* (14), 2991−3002.
(34) Xia, T.; Li, N.; Fang, X. *Annu. Rev. Phys. Chem.* **2013**, *64*, 459−480.
(35) Baigi, M. G.; Brault, L.; Néguesque, A.; Beley, M.; El Hilali, R.; Gaüzère, F.; Bagrel, D. *Toxicol. In Vitro* **2008**, *22* (6), 1547−1554.
(36) Uzdensky, A. B. *Biochem. (Moscow), Suppl. Ser.* **2010**, *4* (1), 3−12.
(37) Okada, C. Y.; Rechsteiner, M. *Cell* **1982**, *29* (1), 33−41.
(38) Jiang, C.; Dou, S.-X.; Wang, P.-Y.; Li, H. *STAR Protoc.* **2022**, *3* (4), No. 101790.
(39) Jiang, C.; Luo, H.-Y.; Xu, X.; Dou, S.-X.; Li, W.; Guan, D.; Ye, F.; Chen, X.; Guo, M.; Wang, P.-Y.; Li, H. *Nat. Commun.* **2023**, *14* (1), No. 5166.
(40) Lai, L.; Jin, J. C.; Xu, Z. Q.; Mei, P.; Jiang, F. L.; Liu, Y. *Chemosphere* **2015**, *135*, 240−249.
(41) Wang, H.; Liu, Z.; Gou, Y.; Qin, Y.; Xu, Y.; Liu, J.; Wu, J. Z. *Int. J. Nanomed.* **2015**, *10*, 5505−5512.
(42) Barros, L. F.; Hermosilla, T.; Castro, J. *Comp. Biochem. Physiol., Part A: Mol. Integr. Physiol.* **2001**, *130* (3), 401−409.
(43) Rello, S.; Stockert, J. C.; Moreno, V.; Gámez, A.; Pacheco, M.; Juarranz, A.; Cañete, M.; Villanueva, A. *Apoptosis* **2005**, *10* (1), 201−208.
(44) Yuan, J. W.; Zhang, Y. N.; Liu, Y. R.; Li, W.; Dou, S. X.; Wei, Y.; Wang, P. Y.; Li, H. *Small* **2021**, *18* (5), No. 2106498.
(45) Guo, M.; Pegoraro, A. F.; Mao, A.; Zhou, E. H.; Arany, P. R.; Han, Y.; Burnette, D. T.; Jensen, M. H.; Kasza, K. E.; Moore, J. R.; Mackintosh, F. C.; Fredberg, J. J.; Mooney, D. J.; Lippincott-Schwartz, J.; Weitz, D. A. *Proc. Natl. Acad. Sci. U.S.A.* **2017**, *114* (41), E8618−E8627.
(46) Jiang, C.; Li, B.; Dou, S.-X.; Wang, P.-Y.; Li, H. *Chin. Phys. Lett.* **2020**, *37* (7), No. 078701.
(47) Li, Y.; Chen, M.; Hu, J.; Sheng, R.; Lin, Q.; He, X.; Guo, M. *Cell Stem Cell* **2021**, *28* (1), 63−78.
(48) Appert-Rolland, C.; Ebbinghaus, M.; Santen, L. *Phys. Rep.* **2015**, *593*, 1−59.
(49) Kanthou, C.; Wei, L.; Surma, M.; Gough, G.; Shi, S.; Lambert-Cheatham, N.; Chang, J.; Shi, J. *PLoS One* **2015**, *10* (7), No. e0131763.
(50) De Vos, K.; Goossens, V.; Boone, E.; Vercammen, D.; Vancompernolle, K.; Vandenabeele, P.; Haegeman, G.; Fiers, W.; Grooten, J. *J. Biol. Chem.* **1998**, *273* (16), 9673−9680.
(51) Wang, Z.; Wang, X.; Zhang, Y.; Xu, W.; Han, X. *Small* **2021**, *17* (11), No. e2005133.

(52) Shen, H.; Tauzin, L. J.; Baiyasi, R.; Wang, W.; Moringo, N.; Shuang, B.; Landes, C. F. *Chem. Rev.* **2017**, *117* (11), 7331−7376.
(53) Risco, C.; de Castro, I. F.; Sanz-Sánchez, L.; Narayan, K.; Grandinetti, G.; Subramaniam, S. *Annu. Rev. Virol.* **2014**, *1* (1), 453−473.
(54) Valm, A. M.; Cohen, S.; Legant, W. R.; Melunis, J.; Hershberg, U.; Wait, E.; Cohen, A. R.; Davidson, M. W.; Betzig, E.; Lippincott-Schwartz, J. *Nature* **2017**, *546* (7656), 162−167.
(55) Li, X. M. *Nat. Methods* **2021**, *18* (5), 440−441.
(56) Li, W.; Kaminski Schierle, G. S.; Lei, B.; Liu, Y.; Kaminski, C. F. *Chem. Rev.* **2022**, *122* (15), 12495−12543.
(57) Gnesotto, F. S.; Mura, F.; Gladrow, J.; Broedersz, C. P. *Rep. Prog. Phys.* **2018**, *81* (6), No. 066601.

https://doi.org/10.1021/acs.analchem.4c00097
Anal. Chem. 2024, 96, 11682−11689